ADVANCED MATERIALS TECHNOLOGIES
www.advmattechnol.de

Microdroplet Magnetic Field Sensor Utilizing Magneto-Birefringence Effect

*Martin Horvat, Patricija Hribar Boštjančič, Darja Lisjak, Alenka Mertelj, and Natan Osterman**

Despite advancements in magnetometry, achieving precise, real-time local magnetic field sensing in microscale systems remains a significant challenge. Here, a compact and versatile magnetic field sensor is presented that utilizes magnetically induced birefringence in micrometer-sized droplets of an isotropic suspension of magnetic nanoplatelets. By measuring the light intensity with crossed polarizers, it is demonstrated that the sensor's capability to detect magnetic fields in the millitesla range with high sensitivity. Experimental results, supported by numerical simulations, confirm the sensor's accuracy and robustness. Its practical application is validated by measuring the magnetic field of a bent current-carrying wire at the microscale. Additionally, a method is introduced for determining both the magnitude and direction of an unknown field using a specialized polarization camera. This novel approach offers a promising pathway for precise, real-time magnetic field sensing in microfluidic and lab-on-chip applications, combining high spatial resolution with optical detection advantages.

1. Introduction

Magnetic field sensing technology plays a crucial role in a wide range of scientific and technological applications, ranging from medical diagnostics to industrial monitoring. The continuous demand for improved sensitivity, reduced size, and enhanced functionality has spurred ongoing research into novel sensor designs. Currently, numerous methods exist for magnetic field measurement – ranging from simple induction-based sensors, such as coils, to advanced superconducting quantum interference devices and resonance magnetometers, which can measure fields as weak as a few femtotesla.[1–3]

Classical magnetic field sensors encompass a diverse range of technologies, with induction coil sensors being widely employed for their simplicity and reliability. Hall effect sensors, utilizing the Hall voltage generated in a conductor subjected to a magnetic field, are prevalent due to their versatility and suitability for various applications. Fluxgate magnetometers, exploiting the magnetic core's saturation characteristics, are commonly used for their accuracy and stability in measuring magnetic fields. Additionally, magnetoresistive magnetometers are technologically very relevant due to their simplicity and cost-effectiveness in various applications: giant magnetoresistance sensors capitalize on the resistance change in multilayer structures subjected to magnetic fields, while anisotropic magnetoresistance sensors, based on the variation in electrical resistance with the angle of magnetic field incidence, have reached 100 times higher field resolution than Hall sensors with the same size and power consumption.[4]

In contrast to classical approaches, quantum sensing methods[5] offer distinct advantages, characterized by superior sensitivity in detecting fields and exceptional spatial resolution in mapping them. Within the array of quantum techniques, nitrogen-vacancy centers in diamonds have risen as a remarkable sensor platform, attaining sensitivities at the picotesla level, achieving nanoscale spatial resolution.[6,7]

Magnetic field sensors utilized across various applications can be susceptible to electromagnetic interferences. An excellent alternative lies in magnetic field sensors utilizing optical detection of magnetic field. This technology is immune to electromagnetic interference, offers remote sensing, can be of compact dimensions and resilient in harsh environments, making it a preferred choice.

Optical readout of magnetic field is typically implemented using optical fibers[8] and magnetic fluid (MF, for a review see, e.g., ref. [9]) as the magnetically sensitive material. MFs exhibits numerous interesting optical properties,[10] including tunable refractive index, tunable transmittance, the Faraday effect, birefringence, dichroism, and the thermal lens effect, among others.

M. Horvat, N. Osterman
Faculty of Mathematics and Physics
University of Ljubljana
Ljubljana 1000, Slovenia
E-mail: natan.osterman@ijs.si
P. H. Boštjančič, D. Lisjak, A. Mertelj, N. Osterman
Jožef Stefan Institute
Ljubljana 1000, Slovenia

The ORCID identification number(s) for the author(s) of this article can be found under https://doi.org/10.1002/admt.202500795

DOI: 10.1002/admt.202500795

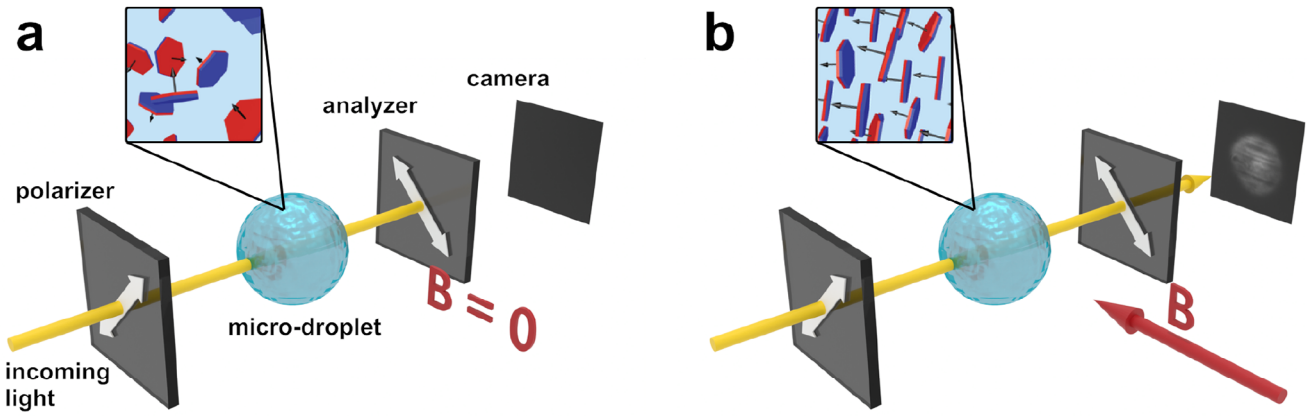

Figure 1. Schematic of the microdroplet magnetic field sensor. A droplet of nanoplatelet suspension is placed between crossed polarizers. a) In the absence of a magnetic field, the suspension is isotropic and does not alter the polarization of the transmitted light. The light is blocked by the analyzer, producing a dark camera image. b) When a magnetic field is applied, the suspension becomes birefringent, converting the incoming linear polarization into an elliptical one. This allows partial transmission of light through the analyzer, resulting in a bright camera image.

Recent advances in two-dimensional nanomaterials have opened new possibilities for magnetic field sensing based on magneto-optical effects, particularly magneto-birefringence and magneto-coloration. These effects enable the visualization and quantification of magnetic fields by analyzing changes in transmitted light intensity, polarization, or color, offering both high sensitivity and intuitive optical readout. Notably, Ding et al. demonstrated a giant magneto-birefringence effect and tunable coloration in suspensions of 2D crystals, enabling direct color-field mapping under moderate magnetic fields.[11] Similarly, Lan et al. reported that collective behavior in 2D inorganic liquid crystals enhances the sensitivity of the magneto-optic response, making them promising candidates for low-field detection.[12] Xu et al. showed that two-dimensional hexagonal boron nitride exhibits magnetically tunable and stable birefringence in the deep ultraviolet range, highlighting its potential for robust optical sensing.[13] Furthermore, size-tuned monolayer 2D materials have been used to modulate magneto-coloration, expanding the design space for magneto-optical sensors.[14]

This manuscript presents a new type a compact and versatile magnetic field sensor, based on magneto-birefringence.[15,16] The core principle of the sensor relies on placing a micrometer-sized droplet of a suspension containing magnetic nanoplatelets between crossed polarizers. When exposed to a magnetic field, the droplet exhibits birefringence, allowing for the measurement of the field strength and direction. The schematic of the sensor is presented in **Figure 1**.

In contrast to classical static sensors, droplets can be generated in large numbers and directed toward specific sensing sites, enabling parallel, localized measurements across a spatially varying magnetic field. Their small volume also reduces thermal and magnetic inertia, allowing for fast response times, as demonstrated in our study. Furthermore, each droplet acts as an independent sensor and can be individually calibrated if needed. The sensor response can be tailored through droplet size, positioning, and suspension composition.

In the absence of an externally applied magnetic field, a MF is an optically isotropic material. However, when the MF is exposed to an external magnetic field, ferromagnetic nanoparticles within it tend to cluster and form chains and columns, aligning along the direction of the magnetic field. As a result, the MF transitions to a new stable state, balancing the thermal energy and magnetic energy of the nanoparticles. The MF can be treated as a traditional birefringent component with optical axes similar to those of an optical uniaxial crystal.

Suspensions of magnetic nanoplatelets (for a review, e.g., see ref. [17]), with their distinct disk-like geometry, offer an even more pronounced birefringent response under an applied magnetic field compared to their spherical counterparts. The high birefringence of these platelets is attributed to the increased optical path differences created by their orientation-dependent refractive indices, which enhance light transmission properties.

The birefringence of nanoplatelets can be expressed as[18,19]

$$\Delta n = \frac{\alpha}{2\, t\, n_{\mathrm{m}}} \Phi S(B) \tag{1}$$

where Φ is volume fraction of nanoplatelets, t and α are their thickness and optical polarizability anisotropy, respectively, and n_{m} mean refractive index of the solution. $S(B)$ is the second order parameter, which depends on magnetic dipole moment p_m and magnetic field density B since the orientational distribution of platelets is given by the Boltzmann distribution as

$$f(\vartheta) \propto \exp\left(\frac{p_{\mathrm{m}} B}{k_{\mathrm{B}} T} \cos\vartheta\right) \tag{2}$$

and

$$S(B) = \langle P_2(\cos\vartheta)\rangle \tag{3}$$

where ϑ is the angle between the field direction and an individual magnetic moment and P_2 is the second Legendre polynomial. By

evaluating the above equation for the given distribution, we get the following expression for the second order parameter,

$$S(b) = 1 + \frac{3}{b^2} - \frac{3}{b}\coth b \tag{4}$$

where $b = \frac{p_m B}{k_B T}$ is dimensionless magnetic field.

2. Results and Discussion

2.1. Birefringence Measurement

The suspension used in the experiment was a 13 g/L dispersion of barium hexaferrite nanoplatelets (BHF NPLs), synthesized hydrothermally in-house following a well-established protocol.[20] The NPLs had a mean equivalent diameter of 50 nm with a standard deviation of 18 nm, and thickness of approximately 4–5 nm as determined from TEM image analysis. Their saturation magnetization, measured by vibrating-sample magnetometry, was approximately 38 Am^2/kg.

We measured the magnetic field-dependent birefringence by placing the suspension into a 500 µm-thick glass capillary and applying a magnetic field at an angle $\theta = 45°$ with respect to the crossed polarizers. The transmitted light intensity, captured using a grayscale camera (UI-3370CP-M-GL, IDS Imaging) mounted on a Nikon Eclipse Ti2 microscope, is then described by the relation:

$$I = I_0 \sin^2(2\theta)\sin^2(\pi d\Delta n(B)/\lambda) \tag{5}$$

If we insert a quarter-wave plate between the polarizer and the sample, with one of its principal axes along the polarization direction, the above equation changes to

$$I = I_0 \sin^2(2\theta)\sin^2(\pi d\Delta n(B)/\lambda \pm \pi/4) \tag{6}$$

where the sign depends on if the axis along the polarization is either slow or fast. This simplifies the measurement of birefringence, since it is easier to encompass the maximum of an expression, which in turn gives value for I_0.

By expressing the Δn from the above equation and measuring the transmitted intensity as a function of applied magnetic field flux density B, we obtain the relation between the birefringence and magnetic field as shown on **Figure 2**. The measurements can be fitted by combining Equations (1) and (4) into

$$\Delta n = \Delta n_s\left(1 + \frac{3}{(p_m\tilde{B})^2} - \frac{3}{p_m\tilde{B}}\coth(p_m\tilde{B})\right) \tag{7}$$

where the saturated birefringence Δn_s and the magnetic moment p_m are fit parameters and $\tilde{B} = B/k_B T$ is magnetic field normalized to the thermal energy. The equation fits the data rather poorly, with values $\Delta n_s = (12.0 \pm 0.3)\cdot 10^{-4}$ and $p_m = (7.1 \pm 0.2)\cdot 10^{-18}$ Am^2. This may be due to the anisotropic absorption of the nanoplatelets or from multiple platelets forming chains, which have a different effect on the birefringence. To account for the latter effect, we fit the data with the sum of two or more terms like from Equation (7). Model with two such terms already fits the data perfectly with values $\Delta n_s^{(1)} = (12.65 \pm 0.08)\cdot 10^{-4}$, $p_m^{(1)} = (4.91 \pm 0.08)\cdot 10^{-18}$ Am^2, $\Delta n_s^{(2)} = (1.5 \pm 0.1)\cdot 10^{-4}$ and $p_m^{(2)} = (2.9 \pm 0.2)\cdot 10^{-17}$ Am^2. The first term with lower magnetic moment can be attributed to single platelet ordering, since its fitted value for magnetic moment is of the same order as reported in ref. [21]. The discrepancy between the actual value may be due to larger clustered structures. We try to describe these by the second term in fit function, which has larger magnetic moment and lower birefringence.

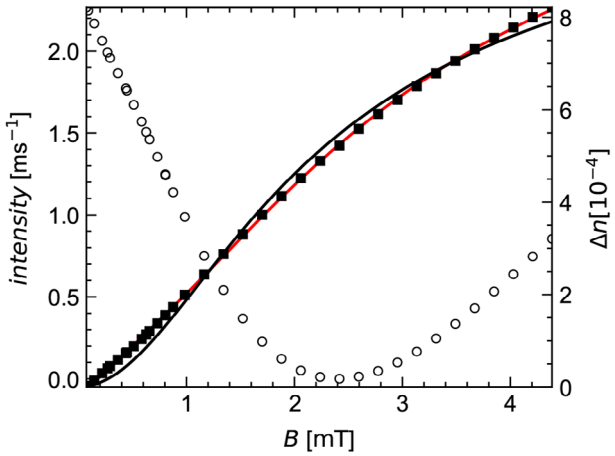

Figure 2. Field-induced birefringence of the material. The measured transmitted light intensity under crossed polarizers I (open circles) and birefringence Δn of the suspension (black squares) as a function of the applied magnetic field density, calculated from (6). The black and red lines represent fitted Equations (1) for single and two platelet types, respectively.

2.2. Light Transmission Through a Droplet Under Crossed Polarizers

Microdroplets were created by pipetting approximately 1 µl of the suspension into 500 µl of paraffin oil. The mixture was then thoroughly stirred, resulting in the formation of droplets used in the subsequent experiments. The smallest droplets generated by this method had a diameter of approximately 50 µm.

While droplets were generated through mechanical mixing, the diameter of each droplet was individually measured before use, and this value was incorporated into the interpretation or calibration of the optical response. Therefore, variations in droplet size did not compromise the accuracy of the sensor. In future implementations, microfluidic droplet generators could be employed to produce highly uniform droplets on demand, improving reproducibility and automation.

Bright-field and polarized images of one such droplet in the presence of a magnetic field are shown in **Figure 3**a,b. The field-induced birefringence is clearly visible as a nonzero intensity inside the droplet in the image taken with crossed polarizers.

We measured light transmission with crossed polarizers for different size droplets by pipetting a mixture of them in a paraffin oil onto a silanized glass. The magnetic field was applied in plane at an angle of 45° to the polarizer direction. We then captured an image and measured the average intensity of the central area inside the droplet. The intensity was then normalized by dividing it with the camera exposure time to allow for a higher dynamic

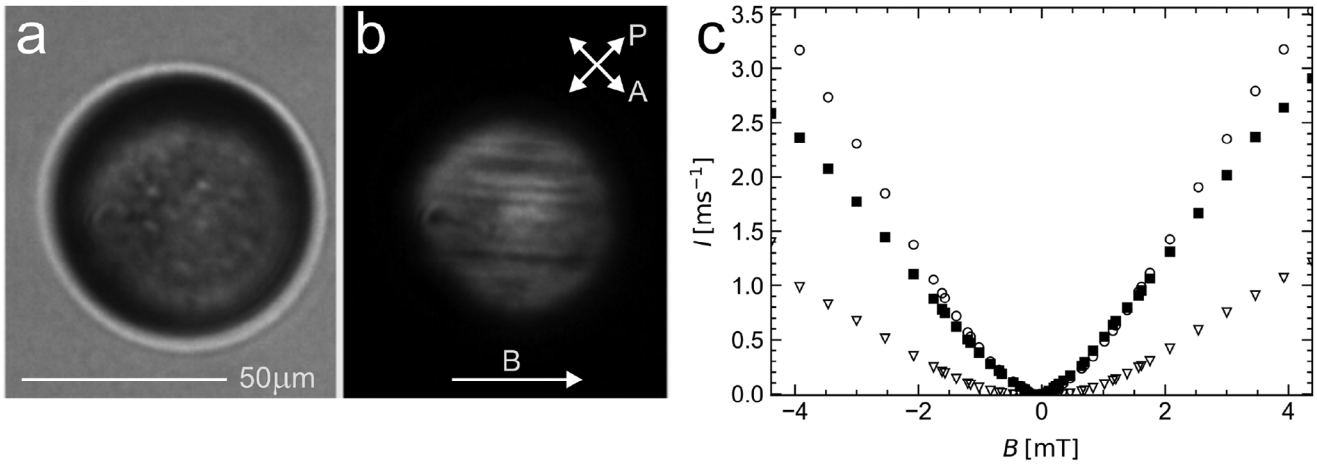

Figure 3. Microdroplets in a magnetic field. a) Bright-field image of a droplet in the absence of an external field. b) Image under crossed polarizers of the same droplet in the presence of an external magnetic field. The arrows indicate the directions of polarizer, analyzer, and magnetic field. c) Transmission under crossed polarizers through droplets with diameters of 87 μm (triangles), 109 μm (squares) and 121 μm (circles) as a function of magnetic field density.

range. Examples for three such measurements are presented in Figure 3c, where the droplet diameters are 87, 109, and 121 μm. As expected, the response is strongly size-dependent.

2.3. Simulation

The simulation of the magnetic droplet sensor was conducted using Nemaktis software[22,23] to model the optical response of the system under various magnetic field configurations. In the simulation, the droplet was represented as a sphere of birefringent material, with the optical axis oriented oriented at 45 degrees with respect to the polarizer. The surrounding medium was treated as an isotropic material, ensuring a realistic representation of the experimental setup. The interaction of polarized light with the modeled droplet was analyzed to predict the intensity distribution observable under crossed polarizers.

The simulation box of 150 × 150 × 150 μm^3 was designed to accommodate droplets of different sizes and ensure boundary effects were negligible, providing an accurate depiction of the optical response within the droplet. In the simulation, we varied the birefringence Δn of the material, and the algorithm calculated the corresponding image of the droplet viewed through crossed polarizers. To quantify the optical response, we averaged the transmitted intensity over the central region of the simulated droplet image, obtaining intensity I as a function of Δn. In the final step, we determined the magnetic field B required to achieve a given birefringence using bi-particle fit in Figure 2.

The results, presented in **Figure 4**, depict the simulated transmitted intensity as a function of the applied magnetic field for three different droplet sizes, exhibiting strong agreement with the experimental data of Figure 3c. At low field strengths, up to approximately 1 mT, the response follows a parabolic functional dependence. Beyond this threshold, the response transitions to a linear dependence on the magnetic field. This behavior arises from the non-linear dependence of the material's birefringence on the applied field (Figure 2), where the birefringence is initially linear to the field, while in higher fields, birefringence saturates.

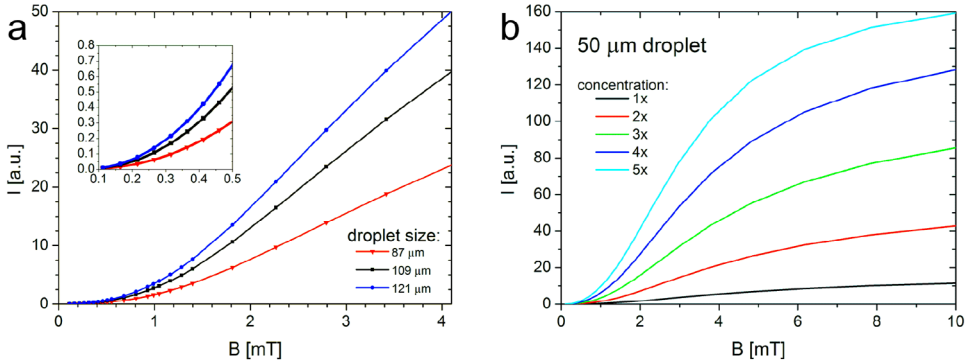

Figure 4. Simulated transmission with crossed polarizers as a function of the applied magnetic field. a) Simulation of the experimental data from Figure 3c: transmitted intensity through droplets with diameters 87, 109, and 121 μm. The inset shows the response at low fields. b) Simulated transmission through a 50 μm droplet of varying platelet suspension concentrations. The black line (1x) denotes the concentration used in the experiment (13 g/L), while the other colors correspond to multiples of this concentration.

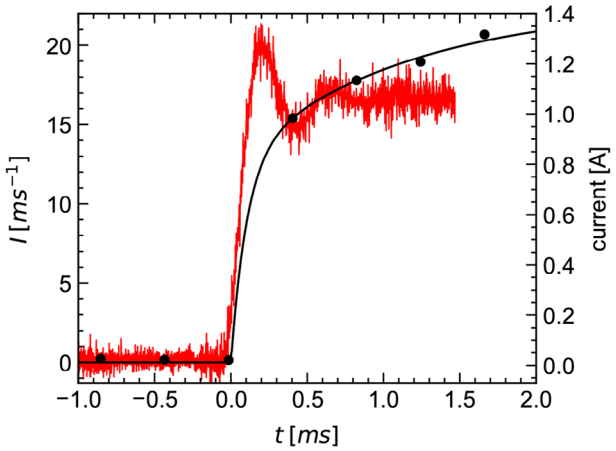

Figure 5. Intensity of transmission under crossed polarizers (black circles) through a droplet and the electric current through the coils (red) after the magnetic field is turned on. The black line represents an exponential fit given by $I = A_1(1 - e^{-t/\tau_1}) + A_2(1 - e^{-t/\tau_2})$, where $\tau_1 \approx 0.1$ ms and $\tau_2 \approx 1.15$ ms.

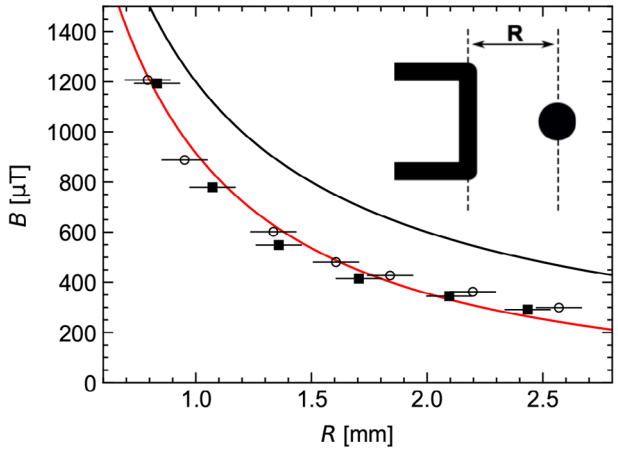

Figure 6. Probing the magnetic field of a bent current-carrying wire at the microscale. Measured magnetic flux density as a function of the distance between the droplet and the wire, as indicated in the inset. Circles and squares represent two sets of measurements performed using the same droplet and wire. The black line corresponds to the theoretical magnetic field of an infinite wire, while the red line includes corrections for the actual wire geometry, as illustrated in the inset.

One possible way to enhance the sensitivity of the sensor is to use a more concentrated suspension of nanoplatelets, thereby increasing the birefringence of the material. In the experiment, we used a concentration of 13 g/L, which remains well below the isotropic-to-nematic transition of BaHF nanoplatelets, occurring at approximately 200 g/L. To investigate the effect of concentration on the sensor response, we performed simulations for 50 μm droplets filled with suspensions of varying nanoplatelet concentrations, ranging from 13 g/L (1x) up to 65 g/L (5x the experimental concentration). In our simplified model, we assumed that the saturated birefringences $\Delta n_s^{(1)}$ and $\Delta n_s^{(2)}$ are directly proportional to the nanoplatelet concentration.

The simulation results shown in Figure 4b indicate that higher birefringence leads to an increased response, with the transmitted intensity exhibiting a stronger dependence on the applied magnetic field. Specifically, at low field strengths, the parabolic regime becomes more pronounced, while at higher fields, the linear response is steeper for suspensions with greater birefringence. These findings suggest that optimizing the nanoplatelet concentration can significantly improve the sensitivity and dynamic range of the birefringence-based magnetic field sensor, providing a potential approach for fine-tuning its performance in microfluidic applications.

2.4. Measurement of the Sensor Response Time

To determine the response time of the droplets, we applied a step current to the magnetic field-generating coils while simultaneously measuring the transmission intensity through a droplet under crossed polarizers. Additionally, we measured the response of the coils to the applied current and confirmed that it was sufficiently fast. This ensured that the observed transition time of the droplets was not limited by the coil response, as illustrated in **Figure 5**.

The response time was found to be independent of the droplet radius. The measured intensity was best described by a biexponential fit

$$I = A_1(1 - e^{-t/\tau_1}) + A_2(1 - e^{-t/\tau_2}) \quad (8)$$

since the data could not be fitted with only one relaxation term. The two time constants were found to be $\tau_1 \approx 0.1$ ms and $\tau_2 \approx 1.15$ ms. These correspond to fast and slow relaxation modes, which can be attributed to the Brownian motion of individual nanoplatelets and self-assembled clusters, respectively. This interpretation aligns with previous findings reported in refs. [24] and [25].

2.5. Magnitude Measurement of a Magnetic Field with a Known Direction

Once the calibration curve for a droplet is established, it can be used to measure magnetic fields at the microscale. We demonstrated this by measuring the magnetic field generated by a short segment of a current-carrying wire, schematically depicted in the inset of **Figure 6**. The wire was positioned such that the generated field was oriented at a 45° angle between the polarizer and the analyzer.

The droplets were placed in a silanized glass cell with a thickness of 200 μm to enable movement toward the cell's edge while minimizing edge lensing effects. The current-carrying wire was then gradually moved away using a translation stage, while the transmitted light intensity through the droplet was recorded. The magnetic flux density was extracted from the calibration curve and compared to analytical predictions for the given geometry. The results showed good agreement within the error margins, which were primarily attributed to the difficulty in precisely determining the wire's center. The measurements, along

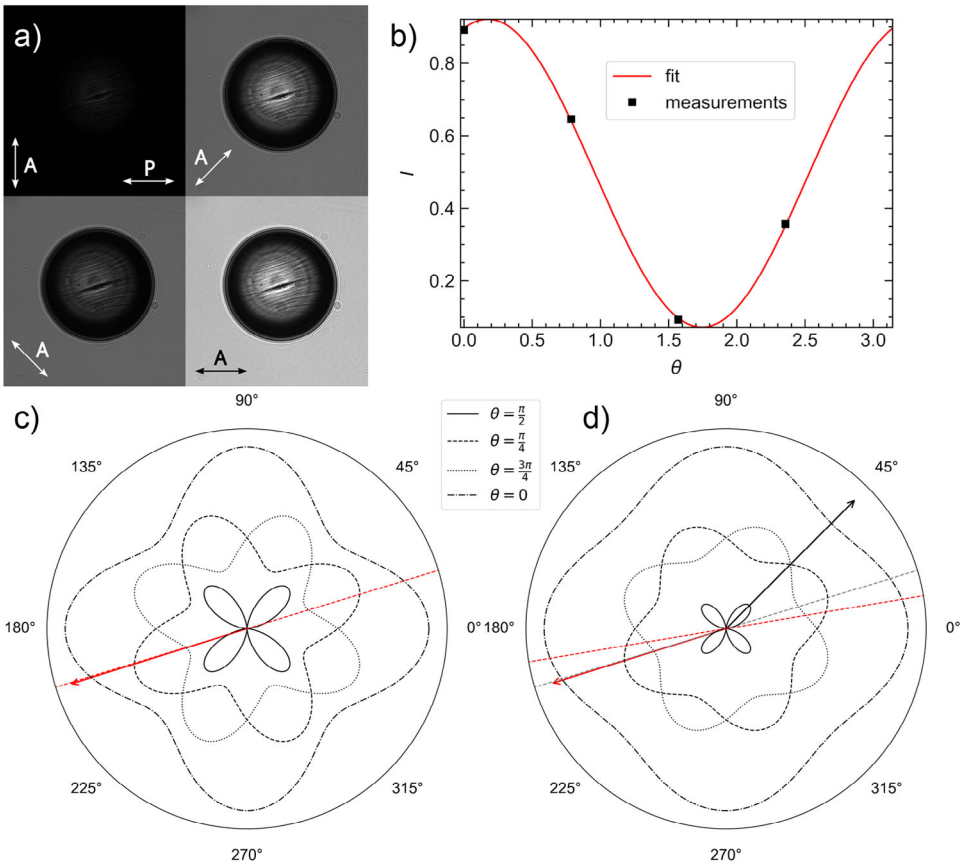

Figure 7. a) PolarSens camera image of a droplet in an external magnetic field of unknown direction and magnitude. The image is divided into four sections, each corresponding to a different analyzer orientation, as indicated by the arrows. b) Fitting Equation (11) to the four intensity measurements obtained at different analyzer orientations reveals two possible solutions for the field direction. c) Polar plot of the intensity as a function of the magnetic field angle ϕ for the four analyzer orientations, with the fit shown as dashed red lines. d) Polar plot after applying an external bias field, indicated by the black arrow. The red arrow represents the direction of the unknown external field. The gray dashed lines indicate the field angle before applying the bias field, while the red dashed lines show the angle after its application.

with the fitted model and geometry schematics, are presented in Figure 6.

2.6. Simultaneous Magnitude and Direction Measurement

Measuring the intensity and determining the magnetic field from the calibration curve of transmission under crossed polarizers is a viable approach only when the direction of the field to be measured is known - a condition that is rarely satisfied in practice.To overcome this limitation, we employ a specialized camera FLIR BlackFly BFS-U3-51S5P-C equipped with a PolarSens image sensor,[26] which captures four intensity values corresponding to different, equally spaced analyzer orientations at each pixel. As a result, the PolarSens camera returns four distinct images, each corresponding to a specific polarization direction, as illustrated in **Figure** 7a.

To derive the detected light intensity, we model the polarization optics using Jones calculus. The initial linear polarization state is represented by a Jones vector (1,0), and its transformation as it passes through the birefringent droplet, rotates due to the optical axis orientation, and encounters the analyzer is described by successive matrix multiplications. Specifically, the sequence involves rotating the coordinate system to align with the optical axis, applying the birefringent phase retardation matrix, rotating back to the laboratory frame, and finally projecting the resulting field onto the analyzer direction. The square of the resulting electric field amplitude yields the transmitted intensity.

The Jones vector at the detector after an analyzer is

$$J' = \mathbf{A}(\theta)\mathbf{R}(-\phi)\mathbf{T}\mathbf{R}(\phi)\begin{pmatrix}1\\0\end{pmatrix} \tag{9}$$

where the incident polarization is along the x-axis, while $\mathbf{A}(\theta)$, $\mathbf{R}(\psi)$ and $\mathbf{T}$ are the Jones matrices for an analyzer rotated by an angle θ with respect to the x-axis, a rotation matrix, and a wave retarder matrix with its fast axis along x-direction, respectively. These matrices are defined as

$$\mathbf{A}(\theta) = \begin{pmatrix}\cos^2\theta & \sin\theta\cos\theta\\ \sin\theta\cos\theta & \sin^2\theta\end{pmatrix}, \quad \mathbf{R}(\phi) = \begin{pmatrix}\cos\phi & \sin\phi\\ -\sin\phi & \cos\phi\end{pmatrix}$$

$$\text{and} \quad \mathbf{T} = \begin{pmatrix}1 & 0\\ 0 & e^{-i\eta}\end{pmatrix} \tag{10}$$

By taking the squared magnitude of the Jones vector J' in Equation 9, we obtain the following expression for the detected intensity:

$$I = I_0[4 + \cos(\eta - 2\theta) + \cos(\eta + 2\theta) - 2\cos(\eta)\cos(2\theta - 4\phi) + 4\cos(2\theta - 2\phi)\cos(2\phi)] \quad (11)$$

where I_0 represents the incident intensity, η is the phase shift between the slow and fast axes of the material, ϕ is the angle of its optical axis, and θ is the angle of the analyzer relative to the incident polarization.

By capturing an image with the aforementioned camera, we obtain intensity measurements for four different analyzer orientations. This allows us to fit the Equation 11 and extract the angle of the material's fast axis. In our case, this corresponds to the angle of the magnetic field density, as our platelets exhibit negative birefringence, with their optical axis aligned along the magnetic field.[21] However, this measurement yields two possible solutions for the angle, differing by 180°. To resolve this ambiguity, we apply a small bias field in a known direction and perform the measurement again. The resulting shift in the measured angle allows us to determine the correct orientation unambiguously.

The external magnetic field before applying the bias field can be expressed as

$$\mathbf{B} = B_0(\cos\phi, \sin\phi) \quad (12)$$

where ϕ is one of the two possible solutions obtained from the fit. After applying the bias field, the total field changes to

$$\mathbf{B}' = B_0'(\cos\phi', \sin\phi') \quad (13)$$

where ϕ' represents the new field orientation.

The relationship between the initial and modified fields is given by

$$\mathbf{B}' = B_0'(\cos\phi', \sin\phi') = B_0(\cos\phi, \sin\phi) + \frac{B_B}{\sqrt{2}}(1, 1) \quad (14)$$

where B_B is the amplitude of the applied bias field, oriented at 45° relative to the incident light.

From this relation, both the field angle and magnitude can be determined by solving the following system:

$$\begin{pmatrix} \cos\phi' & -\cos\phi \\ \sin\phi' & -\sin\phi \end{pmatrix} \begin{pmatrix} B_0' \\ B_0 \end{pmatrix} = \frac{B_B}{\sqrt{2}} \begin{pmatrix} 1 \\ 1 \end{pmatrix} \quad (15)$$

The solutions for ϕ and ϕ' are given by

$$\phi = \phi_0 + \{0, \pi\} \quad \text{and} \quad \phi' = \phi_0' + \{0, \pi\} \quad (16)$$

where ϕ_0 and ϕ_0' are the angles obtained from the fit. Among the two sets of possible solutions, one corresponds to a negative field amplitude, while the other yields a positive amplitude, providing the correct angle. An example of such a measurement is shown in Figure 7.

In the upper left panel (a), an image captured with the polarization camera is displayed, from which four intensity measurements are extracted. These measurements are then fitted using Equation 11, as illustrated in the upper right plot (b). The fitted intensity function for an arbitrary ϕ is shown in the bottom left plot (c), with the calculated ϕ marked by a red dashed line.

Next, an external bias magnetic field is applied, as indicated by the black arrow in the bottom right plot (d), and the measurement is repeated. The resulting angle ϕ differs from the initial measurement, as shown by the gray and red dashed lines in the same plot. From the observed angular shift after applying the bias field, we determine that the correct solution lies in the third quadrant. This yields a final value of $\phi \approx 16.9°$, while the actual applied field angle was $\phi_0 \approx 17.4°$, as indicated by the red arrow in the bottom plots (c,d).

3. Conclusion

We have presented a novel magnetic field sensor based on magnetically induced birefringence in micrometer-sized droplets of an isotropic suspension of magnetic nanoplatelets. By measuring the transmission under crossed polarizers through these droplets, we demonstrated their ability to sense magnetic fields in the millitesla range with high sensitivity. The sensor response was characterized both experimentally and through numerical modeling, showing strong agreement between the measured and simulated results. The observed sensor response exhibited a parabolic dependence at low magnetic field strengths and a linear response at higher fields, in accordance with the nonlinear field dependence of birefringence.

Further, we demonstrated the sensor's practical application by measuring the magnetic field of a bent current-carrying wire on a microscale. The extracted magnetic flux density matched theoretical predictions, confirming the sensor's reliability for localized field measurements. Additionally, the response time of the droplets was found to be on the order of milliseconds, with a biexponential relaxation behavior attributed to the Brownian motion of individual nanoplatelets and their self-assembled clusters.

To enhance the sensor's sensitivity, we explored the effect of varying the nanoplatelet concentration. Simulation results confirmed that increasing the concentration led to a stronger birefringent response, which in turn improved the sensor's detection range and resolution. This suggests that optimizing the suspension composition can further refine the sensor's performance for specific applications.

Beyond measuring magnetic field magnitude, we introduced a method to determine both the magnitude and direction of an unknown field using a specialized polarization camera. By capturing images with multiple analyzer orientations and reconstructing the Jones vector, we resolved the field direction with an accuracy limited only by experimental uncertainties. The inherent ambiguity in determining the field orientation was successfully addressed by applying a small bias field and analyzing the resulting angular shift.

The results presented in this work establish a foundation for utilizing birefringence-based sensors in microfluidic and lab-on-chip applications, where conventional magnetic field sensors may be impractical. Future improvements could focus on enhancing resolution by optimizing nanoplatelet concentration and refining the optical detection setup, as well as extending the detection range for weaker fields. Integrating this approach with

real-time imaging and automated data processing would enable rapid, high-throughput magnetic field mapping at the microscale. Additionally, applying this sensing method to systems, where magnetic interactions play a crucial role, could open new possibilities in soft matter physics, biophysics, and microfluidic sensing technologies.

Acknowledgements

The authors would like to thank Peter Medle Rupnik for his valuable discussions and insightful suggestions throughout this study and Dr. Guilhem Poy for help with Nemaktis package. This work was financially supported by the Slovenian Research and Innovation Agency (J2-50089 and P1-0192).

Conflict of Interest

The authors declare no conflict of interest.

Data Availability Statement

The data that support the findings of this study are available from the corresponding author upon reasonable request.

Keywords

field-induced birefringence, microscale magnetic sensor, microfluidics, nanoplatelets

Received: April 16, 2025
Published online:

[1] J. Lenz, S. Edelstein, *IEEE Sens. J.* **2006**, *6*, 631.
[2] A. Grosz, M. J. Haji-Sheikh, S. C. Mukhopadhyay, *High Sensitivity Magnetometers*, Smart Sensors, Measurement and Instrumentation, vol. *19*, Springer International Publishing, Cham, **2017**.
[3] D. Murzin, D. J. Mapps, K. Levada, V. Belyaev, A. Omelyanchik, L. Panina, V. Rodionova, *Sensors* **2020**, *20*, 1569.
[4] P. Ripka, *J. Magn. Magn. Mater.* **2008**, *320*, 2466.
[5] C. Degen, F. Reinhard, P. Cappellaro, *Rev. Mod. Phys.* **2017**, *89*, 035002.
[6] F. Casola, T. van der Sar, A. Yacoby, *Nat. Rev. Mater.* **2018**, *3*, 1.
[7] E. Marchiori, L. Ceccarelli, N. Rossi, L. Lorenzelli, C. L. Degen, M. Poggio, *Nat. Rev. Phys.* **2022**, *4*, 49.
[8] N. Alberto, M. F. Domingues, C. Marques, P. André, P. Antunes, *Sensors* **2018**, *18*, 4325.
[9] J. Philip, *Adv. Colloid Interface Sci.* **2023**, *311*, 102810.
[10] H. W. Davies, J. P. Llewellyn, *J. Phys. D: Appl. Phys.* **1980**, *13*, 2327.
[11] B. Ding, W. Kuang, Y. Pan, I. V. Grigorieva, A. K. Geim, B. Liu, H.-M. Cheng, *Nat. Commun.* **2020**, *11*, 3725.
[12] T. Lan, B. Ding, Z. Huang, F. Bian, Y. Pan, H.-M. Cheng, B. Liu, *J. Am. Chem. Soc.* **2021**, *143*, 12886.
[13] H. Xu, B. Ding, Y. Xu, Z. Huang, D. Wei, S. Chen, T. Lan, Y. Pan, H.-M. Cheng, B. Liu, *Nat. Nanotechnol.* **2022**, *17*, 1091.
[14] B. Ding, Y. Pan, Z. Zhang, T. Lan, Z. Huang, B. Lu, B. Liu, H.-M. Cheng, *ACS Nano* **2021**, *15*, 9445.
[15] S. Taketomi, *Jpn. J. Appl. Phys.* **1983**, *22*, 1137.
[16] M. Xu, P. J. Ridler, *J. Appl. Phys.* **1997**, *82*, 326.
[17] D. Lisjak, A. Mertelj, *Prog. Mater. Sci.* **2018**, *95*, 286.
[18] S. Neveu-Prin, F. Tourinho, J.-C. Bacri, R. Perzynski, *Colloids Surf. A* **1993**, *80*, 1.
[19] J. Szczytko, N. Vaupotič, M. A. Osipov, K. Madrak, E. Górecka, *Phys. Rev. E* **2013**, *87*, 062322.
[20] P. Hribar Boštjančič, Ž. Gregorin, N. Sebastián, N. Osterman, D. Lisjak, A. Mertelj, *J. Mol. Liq.* **2022**, *348*, 118038.
[21] M. Shuai, A. Klittnick, Y. Shen, G. P. Smith, M. R. Tuchband, C. Zhu, R. G. Petschek, A. Mertelj, D. Lisjak, M. Čopič, J. E. Maclennan, M. A. Glaser, N. A. Clark, *Nat. Commun.* **2016**, *7*, 10394.
[22] G. Poy, S. Žumer, *Opt. Express* **2020**, *28*, 24327.
[23] G. Poy, S. Žumer, *Soft Matter* **2019**, *15*, 3659.
[24] M. Küster, F. Ludwig, A. Eremin, P. H. Boštjančič, D. Lisjak, N. Sebastián, A. Mertelj, H. Nádasi, *J. Mol. Liq.* **2022**, *360*, 119484.
[25] M. Küster, H. Nádasi, A. Eremin, P. H. Boštjančič, F. Ludwig, *J. Magn. Magn. Mater.* **2023**, *588*, 171368.
[26] Sony Semiconductor Solutions, Polarization image sensor technology polarsens™, **2025**, https://www.sony-semicon.com/en/technology/industry/polarsens.html (accessed: April 2025).